Letters

A Dual-Coupled Double-*LCC* System With the Capability of Misalignment Tolerance Improvement for Wireless Charging Substation Inspection Robots

Xiaofei Li, *Member, IEEE*, Fengying Yu, Udaya K. Madawala, *Fellow, IEEE*, Heshou Wang, Hui Feng, Xin Dai, and Jiefeng Hu, *Senior Member, IEEE*

***Abstract*—This article presents a wireless power transfer system for substation inspection robots. Employing a dual-coupled double inductor–capacitor–capacitor (*LCC–LCC*) compensation topology, the system aims to address the prevalent challenge of misalignment tolerance improvements. It reveals that the system's output is predominantly influenced by the denominator parameter (i.e., λ), which is the sum of two dominant factors (i.e., λ_1 and λ_2). Specifically, with larger misalignment, the changing trends of λ_1 and λ_2 are opposite. As a result, their sum (λ) can remain constant by balancing the decrement (increment) in λ_1 with the increment (decrement) in λ_2, thereby achieving a relatively stable power transfer during a certain misalignment range. An experimental prototype is built to verify the effectiveness of the proposed system. The experimental results show that the output current is stable regardless of load variations, and it can also remain stable within the misalignment range of -100 to 100 mm in *y*-axis and 50 to 90 mm in *z*-axis.**

***Index Terms*—Magnetic coupling mechanism, misalignment tolerance improvement, substation inspection robots (SIRs), wireless power transfer (WPT).**

I. Introduction

IN THE realm of power engineering inspection, the advent of substation inspection robots (SIRs) marks a significant leap toward automation [1]. The critical role of inspection robots in power grid maintenance has been gradually underscored these years [2]. Given that these robots predominantly operate in outdoor settings, the conventional approach of contact charging encounters practical limitations. Hence, the adoption of wireless power transfer (WPT) methods to facilitate its efficient functioning has gradually become a trend [3].

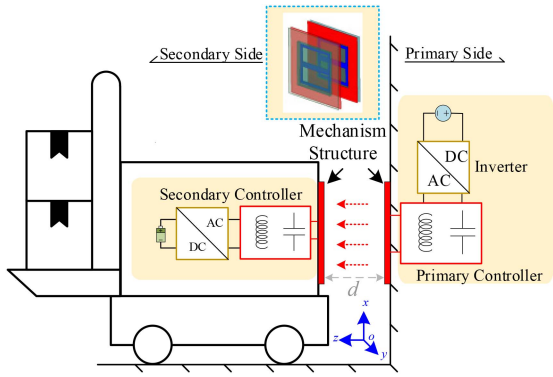

Fig. 1. One typical structure of wireless charging SIRs.

However, a salient challenge hindering the broader application of WPT systems in such scenarios is the stringent requirement for precise alignment between the transmitter and receiver coils [4]. Misalignment, a frequent occurrence in sophisticated environments, such as substations, can drastically reduce the power transfer efficiency, thus impeding the operation of SIRs [5]. In the context of wireless charging for SIRs, attention must be directed towards two axes of misalignment tolerance, specifically the *y*- and *z*-axes, as depicted in Fig. 1. Concerning misalignment in the *x*-direction, it is observed that SIRs typically exhibit minimal variation along this axis. This stability is attributed to the nature of their operational requirements, which do not necessitate cargo transportation; thereby, there is no significant displacement in the *x*-direction.

In the field of wireless charging, a prevalent approach to mitigating misalignments encompasses the integration of control mechanisms within the secondary side of the system. A widely adopted technique involves the incorporation of a dc/dc converter [6]. While effective, this method usually results in a substantial increase in the component's entire size, which is unsuitable for applications in space-constrained environments, such as SIRs [7]. Other methodologies focus on the regulation of the primary side, typically executed by adjusting the phase angle

Manuscript received 4 January 2024; revised 13 February 2024; accepted 5 March 2024. Date of publication 14 March 2024; date of current version 19 April 2024. This work was supported by the National Natural Science Foundation of China under Grant 52007012. *(Corresponding authors: Xiaofei Li; Heshou Wang.)*

Xiaofei Li, Fengying Yu, Hui Feng, and Xin Dai are with the School of Automation, Chongqing University, Chongqing 400044, China (e-mail: xiaofei.li@cqu.edu.cn; fengyingyu@stu.cqu.edu.cn; huif0107@ieee.org; daixin@cqu.edu.cn).

Udaya K. Madawala is with the Department of Electrical Computer and Software Engineering, The University of Auckland, Auckland 1010, New Zealand (e-mail: u.madawala@auckland.ac.nz).

Heshou Wang is with the Department of Electrical Engineering, The Hong Kong Polytechnic University, Hong Kong (e-mail: hs.wang@polyu.edu.hk).

Jiefeng Hu is with the Institute of Innovation, Science and Sustainability, Federation University Australia, Mount Helen, VIC 3353, Australia, and also with the Centre for New Energy Transition Research, Federation University Australia, Mount Helen, VIC 3353, Australia (e-mail: j.hu@federation.edu.au).

Color versions of one or more figures in this article are available at https://doi.org/10.1109/TPEL.2024.3375454.

Digital Object Identifier 10.1109/TPEL.2024.3375454

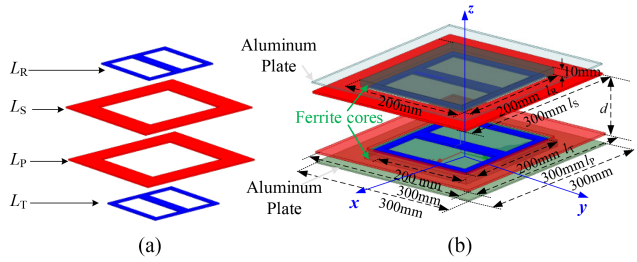

Fig. 2. Magnetic coupling structure. (a) Exploded view. (b) Whole assembly view.

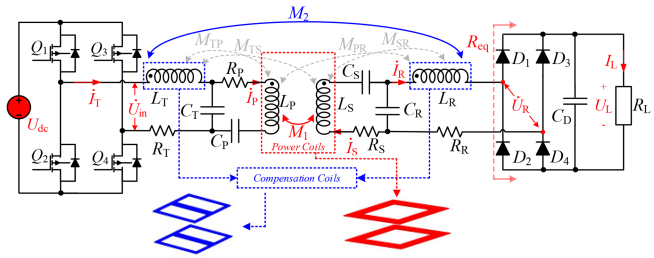

Fig. 3. Circuit diagram of the proposed WPT system.

through the inclusion of an auxiliary wireless communication loop [8]. Nowadays, noncommunication systems with parameter identification capabilities have been used to charge SIRs [5]. However, this approach necessitates the preliminary estimation of mutual inductance values before implementation, thereby introducing an additional layer of complexity to the procedure. In an effort to circumvent the use of controllers, some researchers have concentrated on enhancing anti-offset capabilities through the employment of hybrid compensation topologies [9]. Despite this advantage, it introduces greater complexity into the system. Remarkably, Wu et al. [10] introduced a coupling mechanism designed to maintain anti-offset output under a fixed load. However, its performance may degrade when the load changes.

Considering the challenges previously outlined, this article investigates a double inductor–capacitor–capacitor (i.e., *LCC–LCC*) WPT system with the consideration of dual couplings. In such a topology, the system's output is predominantly influenced by the denominator parameter (i.e., λ), which is the sum of two dominant factors (i.e., λ_1 and λ_2). Specifically, λ_1 demonstrates an upward trend in response to misalignments, while λ_2 exhibits a downward trend. By optimizing the coupling mechanism, the effects of increase and decrease can be neutralized during the misalignment period, thus ensuring a stable sum (λ). A stable λ means a constant output, which will be introduced in Section II. As a result, this stability is maintained despite misalignments happening in the *y*- and *z*-axes. The permissible misalignment range extends up to $\pm$100 mm on the *y*-axis and between 50 and 90 mm on the *z*-axis. The proposed system stands out by offering enhanced misalignment tolerance, allowing for stable output across a broader spectrum of spatial misalignments.

II. Principle Analysis

A. Magnetic Coupling Mechanism

Fig. 2(a) illustrates an exploded view schematic diagram of the coupling mechanism, exclusively showcasing two DD compensating coils (L_R and L_T) and two Q coils (L_P and L_S). Especially, DD coils are bipolar coils, whereas Q coils are unipolar coils, and they can be naturally decoupled with each other after overlapping them together [11]. As a result, the integration of DD and Q coils, realizing an integrated and compact design [12]. Subsequently, Fig. 2(b) presents a comprehensive schematic representation of the entire assembly. Dimensionally, the transmitting and receiving coil (L_P and L_S) measures 300 mm $\times$ 300 mm (i.e., coil size $l_P = l_S = 300$ mm). And the compensation coils (L_R and L_T) exhibit dimensions of 200 mm $\times$ 200 mm (i.e., coil size $l_R = l_T = 200$ mm). The magnetic core, integral to the design, is characterized by dimensions of 200 mm in length and width, with a height of 10 mm. Complementing these components, the aluminum plate incorporated within the mechanism extends to 300 mm by 300 mm, with a thickness of 1 mm. The transmission distance between the transmitting side and the receiving side is *d*.

B. Circuit Analysis

Fig. 3 illustrates the circuit diagram of the proposed WPT system, which employs an *LCC–LCC* configuration.

As can be seen from Fig. 3, the dc input voltage is denoted as U_{dc}. The dc output voltage and current at the load side are represented by U_L and I_L. The self-inductances of two Q (i.e., transmitter and receiver) coils and DD (i.e., compensation) coils are indicated as L_P, L_S, L_T, and L_R, respectively. Their equivalent series resistances are R_P, R_S, R_T, and R_R, respectively.

Noticeably, M_1 is the mutual inductance between L_P and L_S, whereas M_2 is the mutual inductance between L_T and L_R. They play essential roles in stabilizing the output in this article. In addition, C_T, C_P, C_R, and C_S are the resonant capacitors on the transmitting and receiving sides, respectively. And they are designed to satisfy

$$\omega^2 = \frac{1}{C_T L_T} = \frac{1}{C_P (L_P - L_T)} = \frac{1}{C_R L_R} = \frac{1}{C_S (L_S - L_R)} \tag{1}$$

where $\omega = 2\pi f$ is the system operating angular frequency. The operating frequency of the system, *f*, is fixed at 100 kHz and is independent of changes in mutual inductance.

The inverter comprises four MOSFETs, labeled Q_1–Q_4, while the rectifier is constructed using diodes designated D_1–D_4. R_{eq} represents the equivalent input resistance of the rectifier, and R_L denotes the resistance of the load, where they fulfill the relationship as

$$R_{eq} = \frac{8R_L}{\pi^2}. \tag{2}$$

For simplifying the analysis, the fundamental harmonic approximation [3] technique is employed to analyze the system. The fundamental output voltage of the inverter can be solved as

$$\dot{U}_{in} = \frac{2\sqrt{2}U_{dc}}{\pi}\angle 0^\circ. \tag{3}$$

According to Kirchhoff's voltage law, the following equations are able to be obtained as:

$$\begin{cases} \dot{U}_{\text{in}} - j\omega L_{\text{T}}\dot{I}_{\text{T}} - \frac{1}{j\omega C_{\text{T}}}(\dot{I}_{\text{T}} - \dot{I}_{\text{P}}) - j\omega M_2\dot{I}_{\text{R}} - \dot{I}_{\text{T}}R_{\text{T}} = 0 \\ -\frac{1}{j\omega C_{\text{T}}}(\dot{I}_{\text{T}} - \dot{I}_{\text{P}}) + \frac{1}{j\omega C_{\text{P}}}\dot{I}_{\text{P}} + j\omega L_{\text{P}}\dot{I}_{\text{P}} - j\omega M_1\dot{I}_{\text{S}} \\ +\dot{I}_{\text{P}}R_{\text{P}} = 0 \\ \frac{1}{j\omega C_{\text{S}}}\dot{I}_{\text{S}} + \frac{1}{j\omega C_{\text{R}}}(\dot{I}_{\text{S}} - \dot{I}_{\text{R}}) + j\omega L_{\text{S}}\dot{I}_{\text{S}} - j\omega M_1\dot{I}_{\text{P}} + \dot{I}_{\text{S}}R_{\text{S}} = 0 \\ j\omega M_2\dot{I}_{\text{T}} + j\omega L_{\text{R}}\dot{I}_{\text{R}} + \dot{I}_{\text{R}}R_{\text{eq}} - \frac{1}{j\omega C_{\text{R}}}(\dot{I}_{\text{S}} - \dot{I}_{\text{R}}) + \dot{I}_{\text{R}}R_{\text{R}} = 0. \end{cases} \tag{4}$$

Substituting (1) into (4), the following equations are able to be gained as:

$$\begin{cases} \dot{U}_{\text{in}} + \frac{1}{j\omega C_{\text{T}}}\dot{I}_{\text{P}} - j\omega M_2\dot{I}_{\text{R}} - \dot{I}_{\text{T}}R_{\text{T}} = 0 \\ -\frac{1}{j\omega C_{\text{T}}}\dot{I}_{\text{T}} - j\omega M_1\dot{I}_{\text{S}} + \dot{I}_{\text{P}}R_{\text{P}} = 0 \\ -\frac{1}{j\omega C_{\text{R}}}\dot{I}_{\text{R}} - j\omega M_1\dot{I}_{\text{P}} + \dot{I}_{\text{S}}R_{\text{S}} = 0 \\ -\frac{1}{j\omega C_{\text{R}}}\dot{I}_{\text{S}} + \dot{I}_{\text{R}}R_{\text{eq}} + j\omega M_2\dot{I}_{\text{T}} + \dot{I}_{\text{R}}R_{\text{R}} = 0. \end{cases} \tag{5}$$

The parasitic resistances (R_{T}, R_{P}, R_{S}, and R_{R}) are tiny and can be ignored to simplify analysis. Then, the following currents can be gained as:

$$\begin{cases} \dot{I}_{\text{T}} = \frac{\dot{U}_{\text{in}}R_{\text{eq}}}{\omega^2(\frac{L_{\text{T}}L_{\text{R}}}{M_1} + M_2)^2}, \quad \dot{I}_{\text{P}} = \frac{\dot{U}_{\text{in}}L_{\text{R}}}{j\omega(L_{\text{T}}L_{\text{R}} + M_1M_2)} \\ \dot{I}_{\text{S}} = \frac{\dot{U}_{\text{in}}M_1R_{\text{eq}}L_{\text{T}}}{\omega^2(L_{\text{T}}L_{\text{R}} + M_1M_2)^2}, \quad \dot{I}_{\text{R}} = \frac{\dot{U}_{\text{in}}M_1}{j\omega(L_{\text{T}}L_{\text{R}} + M_1M_2)}. \end{cases} \tag{6}$$

The impedance of the inverter can be expressed as

$$Z_{\text{in}} = \frac{\dot{U}_{\text{in}}}{\dot{I}_{\text{T}}} = \frac{\omega^2\left(\frac{L_{\text{T}}L_{\text{R}}}{M_1} + M_2\right)^2}{R_{\text{eq}}}. \tag{7}$$

It can be seen from (7) that Z_{in} is directly influenced by the resistance (i.e., R_{eq}). This indicates that if R_{eq} is exclusively resistive, and Z_{in} will also be accordingly resistive. In order to accomplish zero-voltage switching, the resonant capacitors can be strategically designed with a slightly smaller value than that derived from (1) [13]. By doing this, Z_{in} can exhibit an inductive characteristic.

Next, the relationship between the input and output current of the rectifier can be described as

$$I_{\text{R}} = \frac{\sqrt{2}\pi}{4}I_{\text{L}} \tag{8}$$

where I_{R} is the root-mean-square value of the input current of the rectifier.

Substituting (3) and (8) into (6), I_{L} can be finally expressed as

$$I_{\text{L}} = \frac{4U_{\text{dc}}}{\sqrt{2}\pi\omega\left(\frac{L_{\text{T}}L_{\text{R}}}{M_1} + M_2\right)} = \frac{4U_{\text{dc}}}{\sqrt{2}\pi\omega\lambda}. \tag{9}$$

It can be seen from (9) that I_{L} is independent of the load. Noticeably, there is one key parameter λ that determines the stability of the output current, which can be written as

$$\lambda = L_{\text{T}}L_{\text{R}}/M_1 + M_2 = \lambda_1 + \lambda_2 \tag{10}$$

where key parameter λ can be divided into two subparameters (i.e., $\lambda_1 = L_{\text{T}}L_{\text{R}}/M_1$ and $\lambda_2 = M_2$), which are related to M_1 and M_2. According to (10), although M_1 and M_2 exhibit a decrement with the misalignments in y- and z-axes, an opposite trend is observed in the behavior of λ_1 and λ_2. Specifically, λ_1 demonstrates an increment, whereas λ_2 inversely decreases as the misalignment augments. As long as we optimize the coupling mechanism, their sum λ can remain stable, thereby achieving a stable output current.

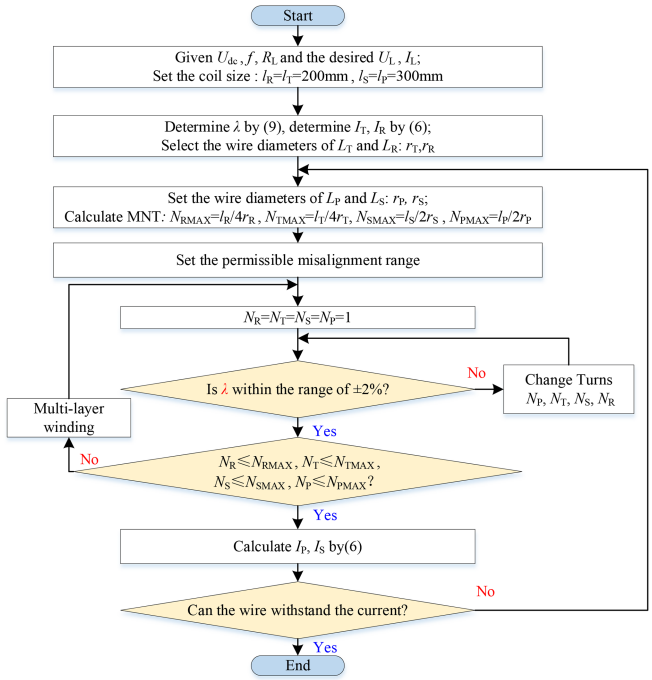

Fig. 4. Design process of the coupling mechanism.

C. Optimization of the Coupling Mechanism

The design process of the coupling mechanism is depicted in Fig. 4 with the help of COMSOL. The constraint on the quantity of coil turns is inherently defined by the predetermined dimensions of the coil and the diameter of the Litz wire. Because the dc voltage source U_{dc}, the operating frequency f, the load R_{L}, the desired outputs (U_{L} and I_{L}), and dimensions (l_{R}, l_{T}, l_{S} and l_{P}) are given, λ can be determined by (9), and I_{T} and I_{R} can be determined by (6). Typically, the selection of the Litz wire diameter is primarily dictated by the current anticipated flowing through the coil. This choice is informed by the fact that Litz wire possesses a relatively high voltage tolerance, making its current-carrying capacity a more critical factor in determining the appropriate wire [14]. Then, the maximum number of turns can be calculated. By adjusting the number of turn numbers (i.e., N_{P}, N_{T}, N_{S}, and N_{R}) for four coils (i.e., L_{P}, L_{T}, L_{S}, L_{R}), λ can remain stable (i.e., within $\pm 2\%$) through a delicate design of the coupling mechanism, which ensures the stable operation of the system under the permissible misalignment range. Finally, the optimized N_{P}, N_{T}, N_{S}, and N_{R} are 18, 4, 18, and 3, respectively.

The experimentally observed variations in M_1, M_2, λ_1, λ_2, and λ are presented in Fig. 5. As can be seen from Fig. 5, although M_1 and M_2 are changing with the misalignments, the parameter λ exhibits stability (i.e., within $\pm 2\%$) over a broad range, because

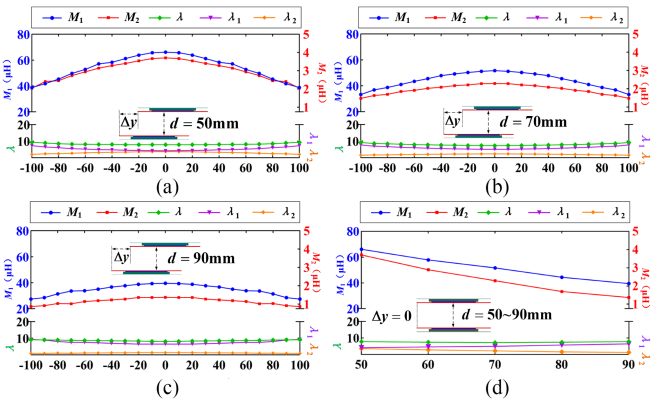

Fig. 5. Variation of the mutual inductance: (a) $d = 50$ mm, Δy (mm), (b) $d = 70$ mm, Δy (mm), (c) $d = 90$ mm, Δy (mm), and (d) $\Delta y = 0$, d (mm), and d is from 50 to 90 mm.

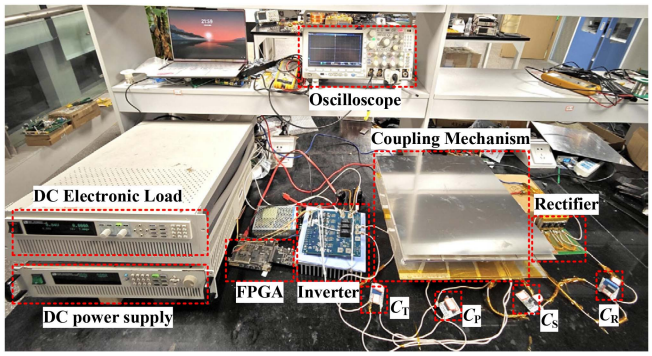

Fig. 6. Experimental setup.

TABLE I
SYSTEM PARAMETERS

L_P	L_S	L_T	L_R	U_{dc}
161.50 μH	159.81 μH	20.95 μH	13.22 μH	70 V
C_P	C_S	C_T	C_R	I_L
16.94 nF	16.86 nF	114.60 nF	180.01 nF	8 A

the changing trends of λ_1 and λ_2 are opposite. The misalignment range is that the transmission distance d varies in the z-direction between 50 and 90 mm, and the lateral displacement Δy in the y-direction ranges from -100 to 100 mm. Moreover, the cross-coupled mutual inductances (i.e., M_{TP}, M_{TS}, M_{PR}, and M_{SR} shown in Fig. 3) are measured as follows: $M_{TP} = 0.17$ μH, $M_{TS} = 0.19$ μH, $M_{PR} = 0.15$ μH, $M_{SR} = 0.16$ μH, they are small enough to be negligible [12].

III. EXPERIMENTAL VERIFICATION

A laboratory setup has been established to validate the proposed system, as shown in Fig. 6. The detailed system parameters are presented in Table I, where U_{dc} is 70 V and the expected output current (I_L) is 8 A. The system is primarily designed for SIRs within a voltage range of 24 [15] to 36 V [5]. Given this voltage specification and the constant current nature of the system, the corresponding load range is within 3 to 4.5 Ω.

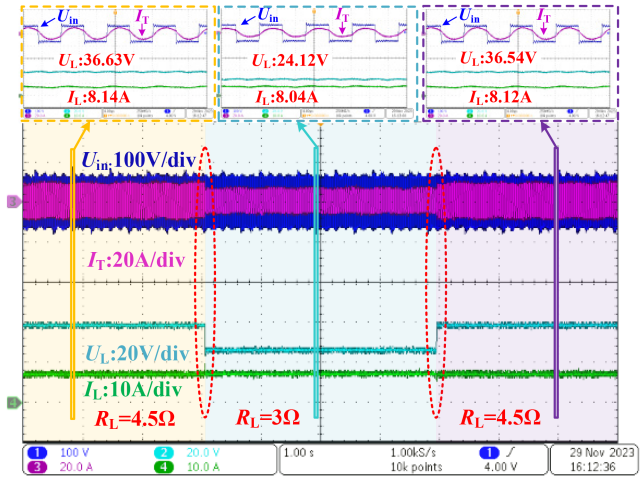

Fig. 7. Dynamic response when the load is changed.

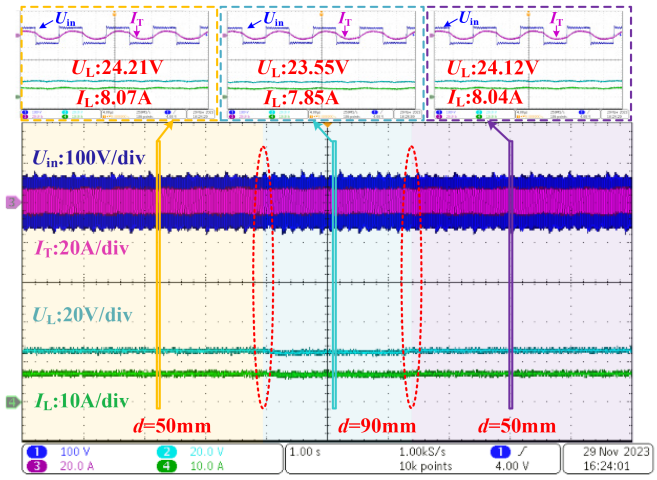

Fig. 8. Experimental validation of the output current (I_L) under the conditions when the transmission distance (d) varies from 50 to 90 mm and returns to 50 mm.

Fig. 7 shows the dynamic response when the load undergoes a transition from 4.5 to 3 Ω, and subsequently returns to 4.5 Ω. It can be seen that the system's dc output current I_L remains relatively stable from 8.14 to 8.04 A, and returns to 8.12 A. Correspondingly, the dc output voltage diminishes in proportion to the decrease in load from 36.63 to 24.12 V, and returns to 36.54 V, thereby confirming the constant current output characteristic. Besides, the system can attain zero voltage switching, as indicated by the slight lag of I_T behind U_{in} [13].

Fig. 8 illustrates the curves of inverter voltage and current output, alongside the load voltage and current, as the longitudinal distance d in the z-direction varies from 50 to 90 mm and then returns to 50 mm. During this variation, the system's dc output current, I_L remains relatively stable from 8.07 to 7.85 A, and returns to 8.04 A, confirming the stability in the response to the dynamic change of d.

Fig. 9 demonstrates the system responses when the y-direction experiences a shift from $\Delta y = 0$ to a maximum offset of 100 mm, followed by a return to the no-offset condition. During this

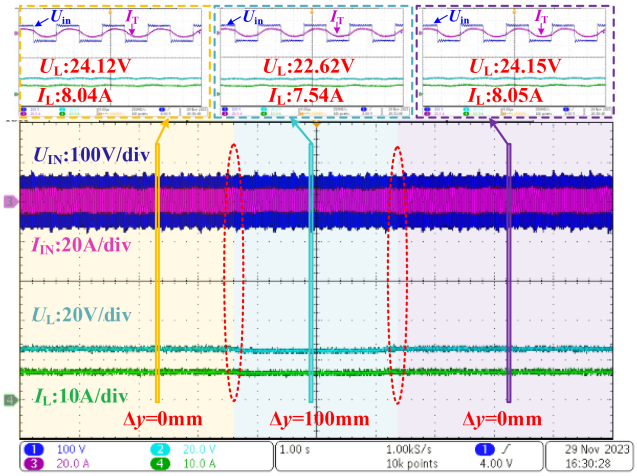

Fig. 9. Experimental validation of the output current (I_L) under the conditions when the y-direction offset (Δy) varies from 0 to 100 mm and returns to 0 mm.

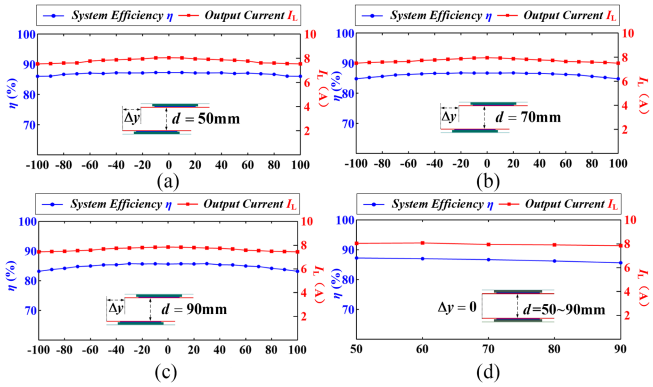

Fig. 10. Experimental validation of the output current (I_L) and measured efficiency under the conditions: (a) $d = 50$ mm, Δy (mm), (b) $d = 70$ mm, Δy (mm), (c) $d = 90$ mm, Δy (mm), and (d) $\Delta y = 0$, d (mm), and d is from 50 to 90 mm.

process, I_L remains relatively stable from 8.04 to 7.54 A, and returns to 8.05 A, verifying the stability of the response to the y-direction misalignment.

Fig. 10 delineates the relationship between system efficiency and output current across various misalignment conditions. The depicted blue curve represents the system efficiency, whereas the red curve corresponds to the output current. Notably, the system achieves its peak efficiency of 87.26% at $\Delta y = 0$ mm and $d = 50$ mm, with an output current of 8.04 A. Next, when $\Delta y = 0$ mm and d is changed from 50 to 90 mm, the efficiency slightly decreases to 85.66%, and the corresponding output current arrives at 7.85 A, aligning with the observations presented in Fig. 8. The minimum efficiency is 83.18%, occurring at $\Delta y = 100$ mm and $d = 90$ mm, with an output current of 7.44 A. Another notable observation is at $\Delta y = 100$ mm and $d = 50$ mm, where the measured efficiency is 86.01% and the measured output current is 7.54 A, which is in agreement with the data presented in Fig. 9.

IV. Discussion

Table II presents the comparison results between the proposed method in this article and those proposed in [5], [7], [8], [9], [10], [16], and [17], which highlights several key advantages and contributions of the presented work. Compared with [5], the proposed system is more straightforward and easier to implement as it eliminates the need for a complex parameter estimation algorithm. Compared with [7], the proposed system is more friendly for SIRs, as it saves the installation space on the secondary side. Compared with [8], the proposed system eliminates the need for an additional communication module. Compared with [9], due to the fact that the proposed system does not require mixing multiple topologies, the topology structure of the proposed system is simpler. Compared with [10], the proposed system is more superior because it can maintain a constant output not only under misalignments, but also under variable load conditions. Compared with [16] and [17], the proposed system is more effective and easier to implement, as it does not require complex control algorithms and avoids the power losses of the switching operations with capacitors or inductors.

TABLE II
Comparisons Between This Article and [5], [7], [8], [9], [10], [16], and [17]

Ref	Type	Method	Characteristic
[5]	Primary-side control	Parameter identification	Complex parameter estimation algorithm
[7]	Secondary-side control	Add DC/DC converter	Increased installation space
[8]	Primary-side control	Wireless communication loop	Additional communication module
[9]	Hybrid-topology	Mixing multiple topologies	Complex compensation topology
[10]	Optimized coupling structure	Antiparallel coils	Fixed load condition
[16]	Secondary-side control	Using variable capacitors	Complex control algorithm
[17]	Secondary-side control	Using variable inductors	Complex control algorithm
This paper	Optimized coupling structure	Dual-coupled LCC-LCC	CC output and no additional control

V. Conclusion

This article presents a novel implementation of a dual-coupled, *LCC–LCC* compensated WPT system. The analysis demonstrates that the output of the system is predominantly influenced by the denominator parameter (i.e., λ), which is the sum of two dominant factors (i.e., λ_1 and λ_2). Specifically, λ_1 demonstrates an upward trend in response to misalignments, whereas λ_2 exhibits a downward trend. Through a delicate design, the parameter λ (i.e., $\lambda = \lambda_1 + \lambda_2$) can be maintained constant, thus achieving a relatively stable power transfer during a wide misalignment range. The experimental evaluation has demonstrated its capability to provide stable and reliable output under various operational conditions. When the load varies between 4.5 and 3 Ω, as well as during misalignments ranging up to ±100 mm in the y-axis and between 50 and 90 mm in the z-axis, the proposed system can maintain a stable 8 A output current with minimal fluctuations.

REFERENCES

[1] H. Liu et al., "Dynamic wireless charging for inspection robots based on decentralized energy pickup structure," *IEEE Trans. Ind. Inform.*, vol. 14, no. 4, pp. 1786–1797, Apr. 2018.

[2] S. Y. R. Hui, Y. Yang, and C. Zhang, "Wireless power transfer: A paradigm shift for the next generation," *IEEE J. Emerg. Sel. Topics Power Electron.*, vol. 11, no. 3, pp. 2412–2427, Jun. 2023.

[3] X. Li, C. Wang, H. Wang, X. Dai, Y. Sun, and A. P. Hu, "A robust wireless power transfer system with self-alignment capability and controllable output current for automatic-guided vehicles," *IEEE Trans. Power Electron.*, vol. 38, no. 10, pp. 11898–11906, Oct. 2023.

[4] H. S. Wang, K. W. E. Cheng, and J. F. Hu, "An investigation of compensation networks for three-coil wireless power transfer," in *Proc. 8th Int. Conf. Power Electron. Syst. Appl.*, 2020, pp. 1–6.

[5] X. Li, H. Wang, F. Zheng, X. Dai, Y. Sun, and A. P. Hu, "Wireless charging of substation inspection robots based on parameter estimation without communication," *IEEE Trans. Circuits Syst. II: Exp. Briefs*, vol. 71, no. 2, pp. 907–911, Feb. 2024, doi: 10.1109/TCSII.2023.3307703.

[6] J. Qi et al., "A multiple-modes resonant switched capacitor DC/DC converter with variable voltage ratios," *IEEE Trans. Power Electron.*, vol. 38, no. 6, pp. 7428–7443, Jun. 2023.

[7] J. Luo, W. Xiao, B. Zhang, D. Qiu, and C. N. M. Ho, "Design of magnetic coupling resonant wireless charging system for cable tunnel inspection robot," in *Proc. IEEE Wirel. Power Transfer Conf.*, 2018, pp. 1–4.

[8] Y. Li et al., "Analysis, design, and experimental verification of a mixed high-order compensations-based WPT system with constant current outputs for driving multistring LEDs," *IEEE Trans. Ind. Electron.*, vol. 67, no. 1, pp. 203–213, Jan. 2020.

[9] L. Zhao, D. J. Thrimawithana, and U. K. Madawala, "Hybrid bidirectional wireless EV charging system tolerant to pad misalignment," *IEEE Trans. Ind. Electron.*, vol. 64, no. 9, pp. 7079–7086, Sep. 2017.

[10] Y. Wu, C. Liu, M. Zhou, X. Mao, and Y. Zhang, "An Antioffset electric vehicle wireless charging system based on dual coupled antiparallel coils," *IEEE Trans. Power Electron.*, vol. 38, no. 5, pp. 5634–5637, May 2023.

[11] H. Wang and K. W. E. Cheng, "Analysis, design, and validation of a decoupled double-receiver wireless power transfer system with constant voltage outputs for industrial power supplies," *IEEE Trans. Ind. Inform.*, vol. 19, no. 1, pp. 362–370, Jan. 2023.

[12] Y. Li, T. Lin, R. Mai, L. Huang, and Z. He, "Compact double-sided decoupled coils-based WPT systems for high-power applications: Analysis, design, and experimental verification," *IEEE Trans. Transp. Electrific.*, vol. 4, no. 1, pp. 64–75, Mar. 2018.

[13] F. Xu, J. Liu, and Z. Dong, "Minimum backflow power and ZVS design for dual-active-bridge DC–DC converters," *IEEE Trans. Ind. Electron.*, vol. 70, no. 1, pp. 474–484, Jan. 2023, doi: 10.1109/TIE.2022.3156159.

[14] C. R. Sullivan and R. Y. Zhang, "Simplified design method for litz wire," in *Proc. IEEE Appl. Power Electron. Conf. Expo.*, 2014, pp. 2667–2674.

[15] R. Guo, L. Han, Y. Sun, and M. Wang, " A mobile robot for inspection of substation equipments," in *Proc. 1st Int. Conf. Appl. Robot. Power Ind.*, 2010, pp. 1–5.

[16] R. Matsumoto and H. Fujimoto, "Wireless EV charging system using PWM-controlled variable capacitor for maximum power transfer under severe coil misalignment," in *Proc. Int. Power Electron. Conf.*, 2022, pp. 1476–1480..

[17] H. Zhang, Y. Chen, D. H. Kim, Z. Li, M. Zhang, and G. Li, "Variable inductor control for misalignment tolerance and constant current/voltage charging in inductive power transfer system," *IEEE J. Emerg. Sel. Topics Power Electron.*, vol. 11, no. 4, pp. 4563–4573, Aug. 2023.